Journal of Fusion Energy (2025) 44:69
https://doi.org/10.1007/s10894-025-00542-y

RESEARCH

Assessment of SPND Signal in IFMIF-DONES using a Monte Carlo Modelling

Irene Álvarez[1,2] · Juan Alejandro de la Torre[1] · Marta Anguiano[1] · Fernando Mota[2] · Concepción Oliver[3] · Axel Klix[4] · Yuefeng Qiu[4] · Dieter Leichtle[4] · Frederik Arbeiter[4] · Santiago Becerril[5]

Received: 1 July 2025 / Accepted: 9 December 2025 / Published online: 18 December 2025

Abstract
IFMIF-DONES (International Fusion Materials Irradiation Facility-DEMO Oriented Neutron Source) is a key facility for the study and analysis of the materials properties exposed to irradiation conditions characterised by a high neutron flux with high energies up to 55 MeV. These irradiation conditions are expected by the future DEMOnstration fusion power plant (DEMO). Within IFMIF-DONES, the irradiation modules which host the specimens material are placed. Therefore, real-time monitoring of the neutron flux is essential to detect and correct any deviations, ensuring continuous and uniform irradiation. Among the diagnostics taken into account, the Self-Powered Neutron Detector (SPND) appears to offer strong physical characteristics in such an environment. However, they have so far only been used in fission reactors. In this work, a theoretical study has been carried out to analyse the signals that could be measured with these diagnostics.

Keywords IFMIF-DONES · Diagnostics · SPNDs

Introduction

The future DEMOnstration fusion reactor (DEMO) will present high-energy neutrons up to 14 MeV with high fluxes up to 10^{15} n cm^{-1} s^{-1} [1–3]. The behaviour of the materials under these irradiation conditions is unknown. Therefore, an intermediate step is needed to study the behaviour of the materials and ensure a safe construction. International Fusion Materials Irradiation Facility-DEMO Oriented Neutron Source (IFMIF-DONES) [4–6] is the intermediate facility which will reproduce the irradiation conditions in DEMO, allowing the study of the material properties. IFMIF-DONES has a deuteron beam (D^+) with 125 mA and 40 MeV, which impacts with a liquid lithium curtain (^{6,7}Li), generating neutrons up to 55 MeV with a broad peak at 14 MeV [7, 8].

The High Flux Test Module (HFTM) [9, 10] is placed inside the IFMIF-DONES and will host the material specimens to be irradiated. This module has a design with 32 rigs, each rig has a hole in the centre to place the diagnostics. Among the diagnostics considered to monitor and control the neutron flux are the ionisation chambers, fission chambers, activation foils, gamma thermometers and thermocouples. However, one of the key diagnostics is the Self-Powered Neutron Detector (SPND) [11]; so, in this study, only this type of diagnostic is considered. In the following sections, the physics of the SPND will be described.

These diagnostics are also considered for the Start-Up and Monitoring Module (STUMM) [12–14]. This module has the similar external design as the HFTM, but inside is full of diagnostics. It will be used in the commissioning phase to characterise the neutron flux and validate the nuclear data libraries.

✉ Marta Anguiano
mangui@ugr.es

1 Department of Atomic, Molecular and Nuclear Physics, University of Granada, UGR, Granada, Spain

2 Laboratorio Nacional de Fusión, CIEMAT, Madrid, Spain

3 CIEMAT, Madrid, Spain

4 Karlsruhe Institute of Technology, KIT, Karlsruhe, Germany

5 IFMIF-DONES España, Granada, Spain

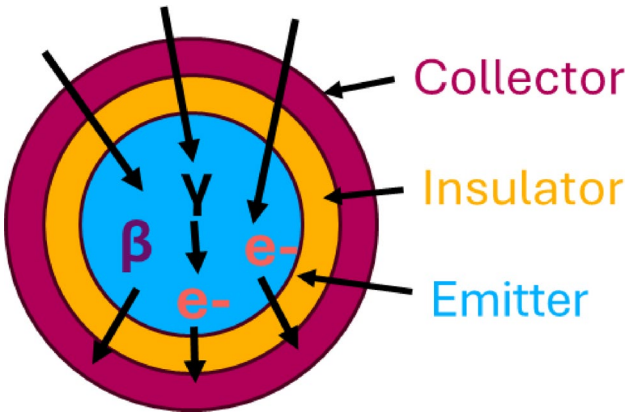

Fig. 1 Horizontal cross section of a cylindrical SPND and the different processes that can occur in order to create current. The components are (n, β^-), (n, γ, e^-) and (γ, e^-)

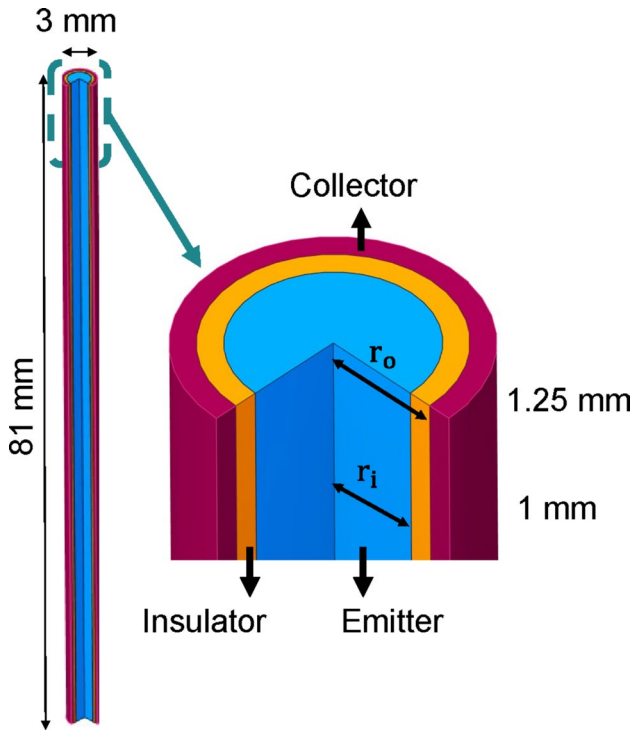

Fig. 2 Details of the geometry used for the SPND simulations. The blue part corresponds to the emitter, the yellow part to the insulator and the red part to the collector

SPND Design and Physics

The SPND is a diagnostic that can measure fluxes of neutrons and photons inside power reactors without an external power supply [11]. It features a multilayer structure composed of two electrodes separated by an insulator. The inner electrode, known as the emitter, generates electrons when exposed to radiation. These electrons pass through the insulating layer and are collected by the outer electrode, or collector (Fig. 1). This electron flow generates a measurable electric current, which is in principle proportional to the neutron flux. SPNDs provide real-time, continuous monitoring of radiation levels in reactor environments.

The signal produced by the SPND consists of three distinct components: one delayed and two prompts.

- Delayed component (n, β^-): In this process, a neutron is absorbed by the emitter material, producing a radioactive daughter nuclide that undergoes β^- decay. Since the signal depends on the half-life of this decay, it does not respond immediately to changes in neutron flux, making it a delayed component.
- Prompt Component (n, γ, e^-): In this mechanism, neutrons interact with the emitter to produce high-energy photons. These photons then produce electrons in the emitter via the photoelectric effect, Compton scattering or pair production. The resulting electrons immediately contribute to the electrical signal.
- Prompt component (γ, e^-): This is where external photons radiation interacts directly with the emitter material. These interactions also produce secondary electrons, which add to the measured signal. High atomic number (Z) materials such as bismuth (Bi) and lead (Pb) are particularly effective in this process due to their higher photon interaction cross sections.

SPNDs offer several advantages as diagnostic tools: they have a compact, rugged design capable of operating at high temperatures and intense neutron and gamma fluxes. Their small size allows them to be placed almost anywhere in a reactor, and they do not require an external bias, taking into account the restrictions imposed by the wire. However, the electrical current generated is very low, typically in the picoampere range, and its sensitivity can degrade over time due to the depletion of the emitter material if used in high flux regions.

The SPND geometry used in this study is shown in Fig. 2. The collector is made of steel, the insulator is alumina, and two emitter materials were considered: rhodium (Rh) and chromium (Cr).

For rhodium, the emitter material used in the SPND is the stable isotope ^{103}Rh, which has a natural abundance of 100% [15]. When it undergoes a neutron capture reaction (n, γ), it produces ^{104}Rh (92.6%) and the metastable isotope ^{104m}Rh (7.4%) [16]. These isotopes have relatively short half-lives of 42.3 s and 4.34 min, respectively. Figure 3 (green line) shows the reaction cross section, which is remarkably high for thermal neutrons, but decreases by three orders of magnitude at 14 MeV.

In the case of chromium, several neutron-induced reactions can lead to β^- decays. Among the Cr isotopic composition, ^{52}Cr is the most abundant isotope, so the most

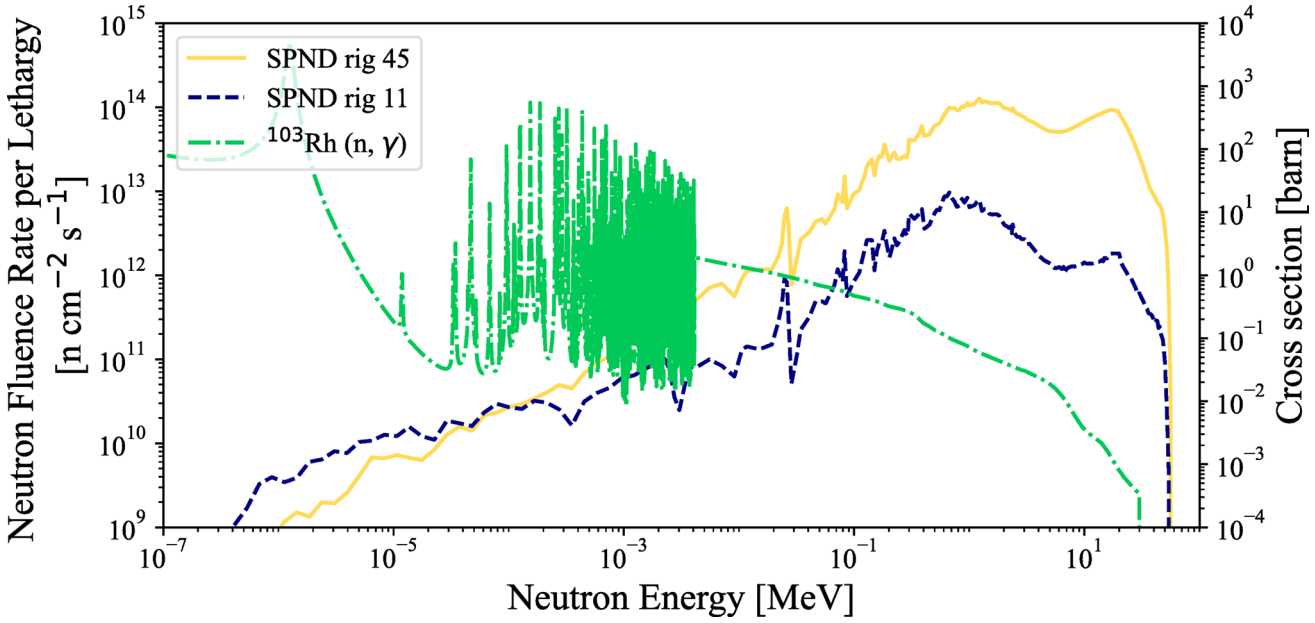

Fig. 3 Neutron fluence rate per unit lethargy [n cm^{-2} s^{-1}] in the SPNDs in rigs 45 and 11 (left axis) versus the cross section ^{103}Rh (n, γ) ^{104}Rh using FENDL.3.1d library (right axis). Obtained with JANIS NEA [17]. All axes are on a logarithmic scale

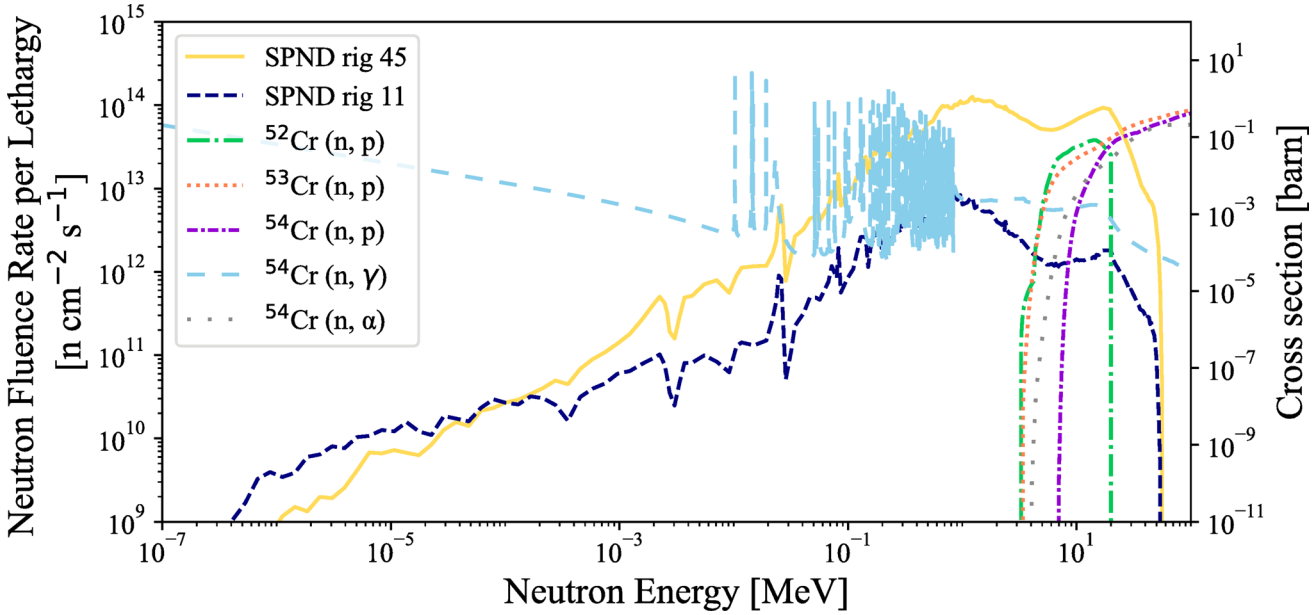

Fig. 4 Neutron fluence rate per unit lethargy [n cm^{-2} s^{-1}] in the SPNDs in rigs 45 and 11 (left axis) versus the cross section Cr reactions using FENDL.3.1d library (right axis). Obtained with JANIS NEA [17]. All axes are on a logarithmic scale

significant is the ^{52}Cr(n, p)^{52}V reaction. The resulting isotopes have relatively short half-lives (minutes), which are negligible in the context of a one-year irradiation period. Figure 4 shows the cross sections for the various reactions. The (n, γ) reaction (cyan line) is more probable with thermal and epithermal neutrons, while the others are threshold reactions that produce gases. These threshold reactions require neutron energies slightly below 1 MeV and exhibit low cross sections, typically under 1 barn.

IFMIF-DONES Conditions

The first two positions analysed correspond to SPNDs placed in rig 45, located in the first row of the HFTM, and rig 11, situated in the last row—farthest from the beam. The specimen model configuration is the CLC.v2.0 [17, 18]. Comparing these two positions provides valuable insight into how the SPND signal varies across the HFTM. Figure 5 presents the HFTM positions in the Test Cell and the two rigs selected for the study.

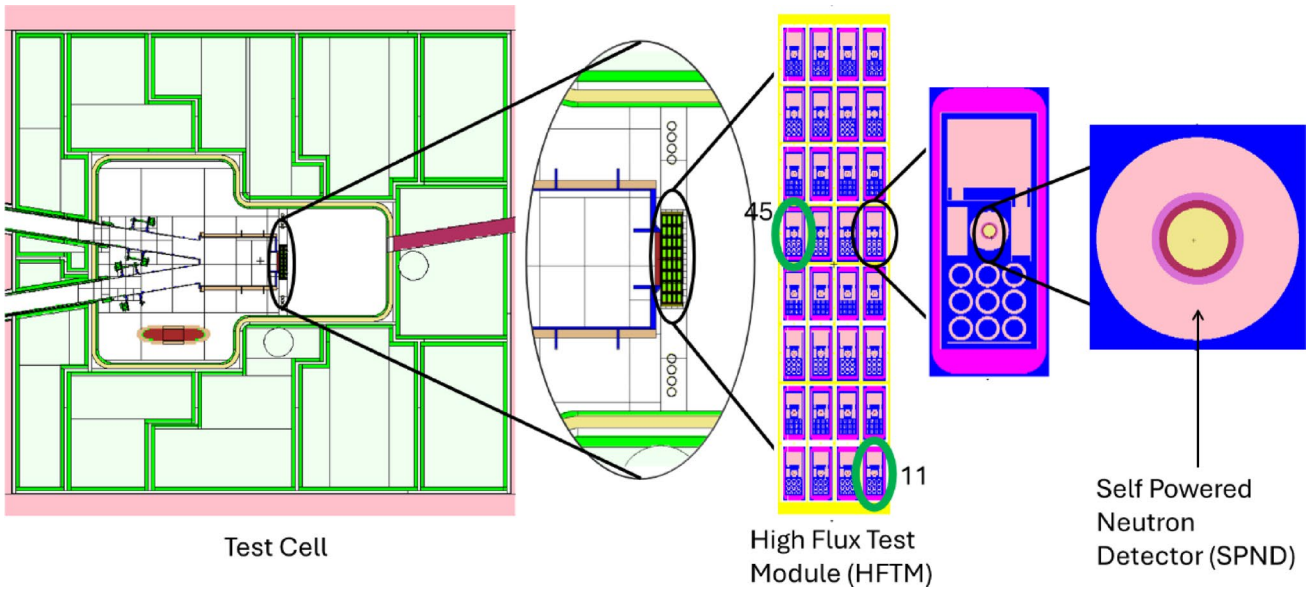

Fig. 5 Test Cell horizontal cross section at z = 0 with the CLC.v2.0 specimen distribution model in the HFTM. SPNDs in rigs 45 and 11 are selected for the signal sensitivity study

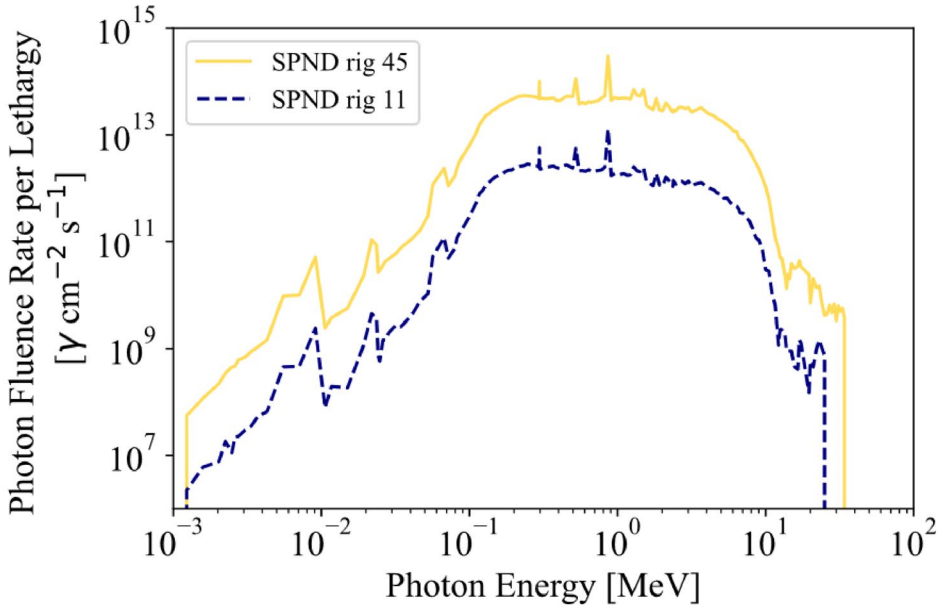

Fig. 6 Photon fluence rate per unit lethargy [γ cm^{-2} s^{-1}] in the SPND in rigs 45 and 11. Both axes are on a logarithmic scale

The photon and neutron spectra used in the analysis are shown in Figs. 3 and 6, and Fig. 4. For the photon spectrum, the SPND located in rig 45 shows a flux up to two orders of magnitude higher than that in rig 11. For the neutron spectrum, the SPND in rig 45 reaches a flux of up to 10^{14} n cm^{-2} s^{-1} in the 14 MeV range, while the SPND in position 11 shows a maximum flux of about 10^{12} n cm^{-2} s^{-1}. Conversely, for neutron energies below 10^{-4} MeV, the flux at rig 11 exceeds that at rig 45. However, in the case of the photon fluence rate, the profiles of the curves are in good agreement, but with a difference of two orders of magnitude.

Figure 3 compares the neutron spectra at positions 11 and 45 with the cross section of ^{103}Rh. The figure shows that this isotope presents a higher cross section for epithermal neutrons than for fast neutrons, supporting its common use in fission reactors [19].

In the case of chromium, as shown in Fig. 4, the threshold energy reactions fall within the range of the peak neutron flux, although their cross section values remain quite low. The only non-threshold reaction, a neutron capture reaction (^{54}Cr(n, γ)), shows significantly higher cross sections at lower neutron energies. Since each material reacts differently depending on the neutron energy spectrum, a

sensitivity study will be carried out for the SPNDs in the two specified rigs to assess how the signal varies with the choice of emitter material.

Beam Footprints

This section introduces and describes the different beam profiles used in the study. The High Energy Beam Transport (HEBT) line is the final subsystem of the accelerator and is responsible for transporting the deuteron beam to the lithium target and shaping it to the reference beam profile using magnetic elements [20].

To focus and centre the beam, the HEBT line contains 18 quadrupole magnets and 12 pairs of horizontal and vertical steering magnets. Two dipole magnets achieve beam deflection, each providing a 4.5º deflection to achieve the total 9º deflection required to direct the beam to the target. In the HEBT final section, dedicated to shaping the beam to the required footprint, the system includes a set of nonlinear magnets: two octupoles and two dodecapoles [20]. As a result, the beam profile is highly dependent on the configuration of these magnetic elements. The arrangement and positioning of the magnets are presented in [21].

The primary beam profile used in this study is IFMIF-EVEDA [22]. The distribution of this profile has two intensity peaks at the edges and one in the centre. In this study, only the standard beam footprint size, 20×5 cm^2, has been considered.

To evaluate the variation in the dose received by the specimens and the resulting diagnostic signal, additional beam profiles beyond the IFMIF-EVEDA baseline were considered for the IFMIF-DONES facility. Beam acceleration and transport are sensitive to various errors in the accelerator components [5, 23]. Of particular concern are magnet and cavity misalignments (displacements and rotations) and field variations due to power supply ripple. Beam dynamics simulations consider two types of errors: static errors, which evolve slowly and can be corrected by tuning, and dynamic errors, which evolve rapidly and are typically caused by factors such as mechanical vibrations due to component cooling. These errors can lead to beam misalignment; emittance coupling and even beam loss.

Four additional beam profiles were considered for this study. The HEBT NOMINAL beam profile (Fig. 7a) is currently under development as an upgrade to the IFMIF-EVEDA one, incorporating recent improvements to the Superconducting Radio Frequency (SRF) linac and the

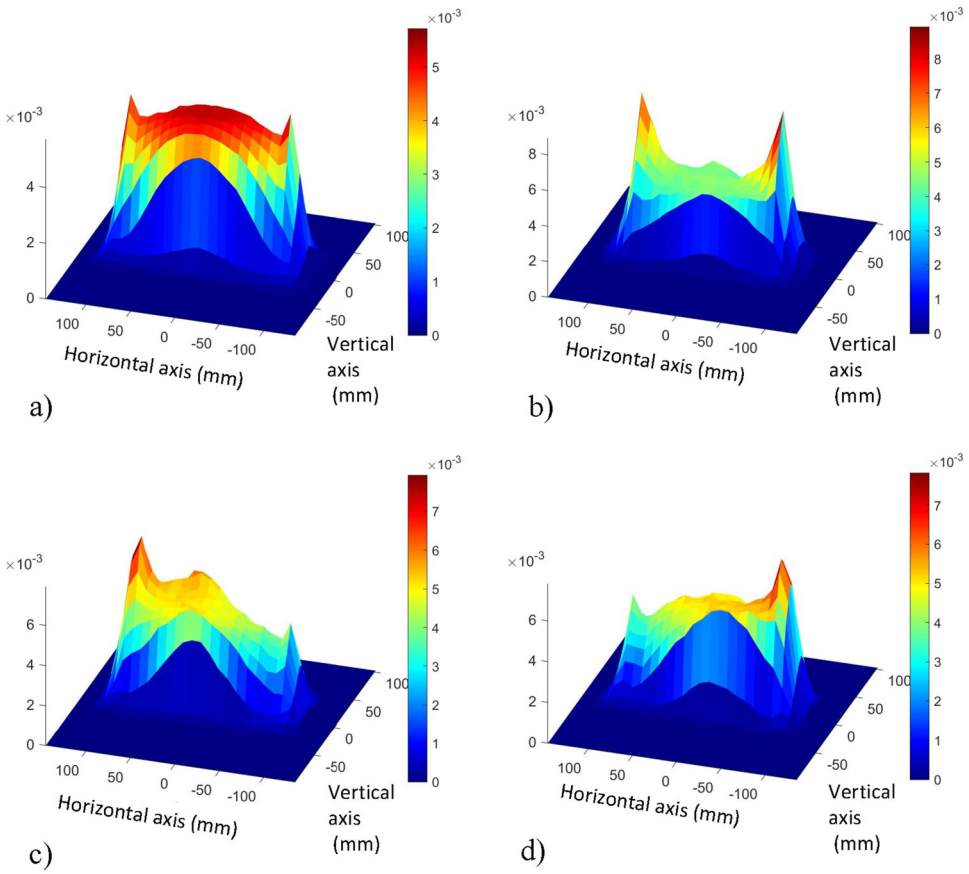

Fig. 7 Deuteron beam profiles with intensity normalised (the sum of all the data equal to 1) with 20×5 cm^2 beam footprint size; (**a**) HEBT NOMINAL (**b**) OCTUPOLEX (**c**) Asymmetric#a and (**d**) Asymmetric#b

HEBT line. It features pronounced side peaks and a broadened central peak.

The OCTUPOLEX beam profile (Fig. 7b) is derived from the HEBT NOMINAL profile by doubling the field strength of the horizontal octupole magnet (OCT-X) from 509.423 T m^{-3} to 1018.85 T m^{-3}. This adjustment significantly increases the side peaks while reducing the centre density. To maintain comparable beam envelope characteristics, the last two quadrupoles (QUAD17 and QUAD18) have been slightly retuned to maintain RMS size.

The Asymmetric#a and Asymmetric#b beam profiles (Fig. 7c and d) are examples that show the beam distortion caused by static and dynamic component errors. Asymmetric#a shows a density shift towards the positive y-axis, while Asymmetric#b shows the opposite, concentrating the beam intensity in the negative y-axis region. These profiles simulate realistic beam deviations due to magnet misalignment or dynamic instabilities and highlight potential asymmetries that may occur during normal operation.

Understanding how these profiles affect both the neutron field and the SPND responses is essential for evaluating the feasibility of using SPNDs for online beam monitoring and diagnostics in IFMIF-DONES. In all the cases, the beam intensity is the same but with a different distribution.

Methodology

A number of theoretical and analytical models have been developed to estimate the electrical signal produced by self-powered neutron detectors (SPNDs) [24–28]. This paper presents an SPND model implemented in MCNP, based on the approach proposed by P. Raj [11]. The version used is MCNP6.2 [11] with the nuclear data library FENDL.3.1d [31].

To apply this model, it is necessary to input the neutron and gamma spectra at the SPND location, as well as the total neutron fluence rate ($\dot{\phi}$) incident on the detector. In addition, the geometry and material composition of the SPND must be defined. The analysis is divided into three steps, each corresponding to a different component of the signal, as explained above.

- (n, β^-): The first step is to calculate the number of unstable nuclei produced in the emitter using the neutron spectrum as a source. As MCNP does not track radioactive decay, an additional step is required to estimate the resulting charge deposition. In this step, the neutron fluence incident on the SPND surface (φ) is also obtained.

  In a second simulation, the reaction rate for the production of unstable nuclei is used to define an isotropic electron source, the energy of which is derived from the beta spectrum of the resulting isotope. This allows the calculation of the charge deposited in the SPND layers by this process (Q_β).

- (n, γ, e^-): The prompt signal generated directly by neutrons is calculated using the neutron spectrum as a source, allowing the charge deposited in each SPND layer to be determined directly (Q_n).
- (γ, e^-): This component is evaluated in a similar way to the neutron prompt signal, but using the gamma spectrum instead. The resulting deposited charge is the gamma contribution (Q_γ).

The following procedure is used to calculate the charge deposited by each component. The emitter cylinder is divided into ten concentric inner cylinders to improve the resolution of the reaction rate within this layer. For each charge component (Q), the net electron flux in both the emitter and insulator cylinders and the F factor must be considered into account. The F factor takes into account the space charge effect within the insulator. As electrons move away from the emitter surface, some will occupy interstitial sites in the insulator material, creating an electrostatic field along their path. If the charge distribution within the insulator is nearly uniform, the electric potential across its thickness forms a parabolic profile, with the electric field crossing zero at the inversion point.

If an electron crosses this inversion point, the induced field drives it towards the collector, contributing to the signal. If the electron fails to cross the inversion point, due to insufficient energy or a complex trajectory, it is slowed down and pushed back towards the emitter, effectively negating its contribution to the signal. As a result, the charge is modified by a return factor that accounts for the space charge effect.

$$Q = e(Q_{\text{emitter}} + F\, Q_{\text{insulator}}), \tag{1}$$

where F is calculated as:

$$F = \frac{\log(r_o)}{\log\left(\frac{r_o}{r_i}\right)} - \frac{1}{\log\left(\frac{r_o}{r_i}\right)} \frac{\int_{r_i}^{r_o} r \log(r)\ \rho\ (r)\ dr}{\int_{r_i}^{r_o} r\, \rho\ (r)\ dr}, \tag{2}$$

where:

r_o is the outer radius of the insulator.

r_i is the inner radius of the insulator.

ρ is the charge density of the insulator.

But, it has been found that F can be considered constant in this study, as indicated by previous studies [32]:

Table 1 Measured and estimated electrical current for two Rh SPNDs in the BR2 reactor at channels E30 and L180. 'The numbers between parentheses indicate the uncertainty with a coverage factor k = 1; that is, 1.012(5) means 1.012 ± 0.005'

Electrical currents				
	Channel E30 [μA]	Relative variation [%]	Channel L180 [μA]	Relative variation [%]
Measured current	2.64		0.93	
MCSS calculation [19]	2.65	0.38	0.94	1.08
Goldstein calculation [33]	2.06	−21.97	0.74	−20.43
Analytical model calculations [26]	3.05	15.53	1.08	16.13
This work calculations	2.978(15)	12.80	1.082(5)	16.34

$$F = \frac{\log(r_o)}{\log\left(\frac{r_o}{r_i}\right)} - \frac{1}{\log\left(\frac{r_o}{r_i}\right)} \frac{r_o^2 \log(r_o) - r_i^2 \log(r_i) - \frac{r_o^2 - r_i^2}{2}}{r_o^2 - r_i^2}. \quad (3)$$

After calculating the charge for each component, the overall charge will be obtained by adding the contribution of all of them:

$$Q_t = Q_\beta + Q_n + Q_\gamma \quad [A\,s]\,. \quad (4)$$

And from the charge, the sensitivity can be calculated:

$$S = \frac{Q_t}{\phi} \quad \left[A\,cm^2\,s\,n^{-1}\right], \quad (5)$$

where φ is the neutron flux on the surface of the detector in [n cm^{-2}]. The total estimated electrical current is given by:

$$I = S\,\dot{\phi} \quad [A]\,, \quad (6)$$

where $\dot{\phi}$ is the neutron fluence rate [n $cm^{-2}\,s^{-1}$].

Validation of the Methodology

In this paper, the method described above is used to estimate the electric current generated by the SPND. The signal depends not only on the position of the SPND ($\dot{\phi}$) but also on the material used for the emitter (Q).

The BR2 experimental data used to validate the method are presented in [19]. The paper provides a comprehensive set of experimental and theoretical data obtained by alternative methods. The models considered for comparison with our data include the Warren model [26] (referred as the analytical model), the Goldstein model [33] and the MCSS model [19].

The experiment was conducted in the BR2 reactor [19], where the electrical signal was measured by two Rh SPNDs positioned at different locations in the reactor, specifically in channels E30 and L180. These channels have neutron fluence rates of $8.9{\cdot}10^{14}$ and $2.8{\cdot}10^{14}$ n $cm^{-2}\,s^{-1}$, respectively [19].

Table 2 Estimated electrical current for the cr and Rh SPNDs in positions rig 45 and 11. Data are presented in total and by component. The numbers between parentheses indicate the uncertainty

Estimated current [nA]				
Emitter material	Cr		Rh	
Rig	11	45	11	45
(n, β^-)	0.2400(2)	10.890(8)	10.33(6)	86.3(2)
(n, γ, e^-)	1.42(18)	68(5)	2.34(13)	93(4)
(γ, e^-)	23.38(35)	576(8)	21.79(3)	523(8)
Total	24.8(5)	644(11)	34.6(5)	703(12)

Performing the calculations based on the methodology described above, the data presented in Table 1 are obtained, together with the other results of the study. The estimated signals in this work are very close to those derived from the analytical model, with deviations from the measured current of 12.8% for channel E30 and 16.34% for channel L180.

The data closest to the experimental results comes from the MCSS model. However, it is important to note that some experimental information is missing, which hinders the ability to reproduce the experiment in BR2 with high accuracy [19]. The MCSS method, based on the MCNP code, relies on a nuclear data library for neutron transport, but the specific library used is not specified. In addition, there is no information on the uncertainties associated with the theoretical models or the experimental data. Even taking these factors into account, the order of magnitude of simulated currents were correctly reproduced allowing to consider the SPND model here used well validated.

Results

The corresponding electrical signals have been estimated by applying the proposed methodology to an SPND with the specified characteristics, positioned at rigs 11 and 45 within the HFTM. These results enable a comparative analysis of signal intensity as a function of both spatial location and emitter material.

Table 2 presents the estimated results for IFMIF-DONES. The dominant signals at both positions are the prompt contributions, as presented in [8]. Regarding the beta decay contribution, in the Rh SPND, it becomes more significant than in the Cr case, reaching 10% of the total. In both positions, the total signal of the Rh SPND is higher than that of the Cr SPND. In addition, the signals in rig 11 are about ten times lower than those in rig 45, highlighting a noticeable variation due to the difference in position.

However, using the spectrum as an isotropic source is not the most realistic approach. The phase space of neutrons

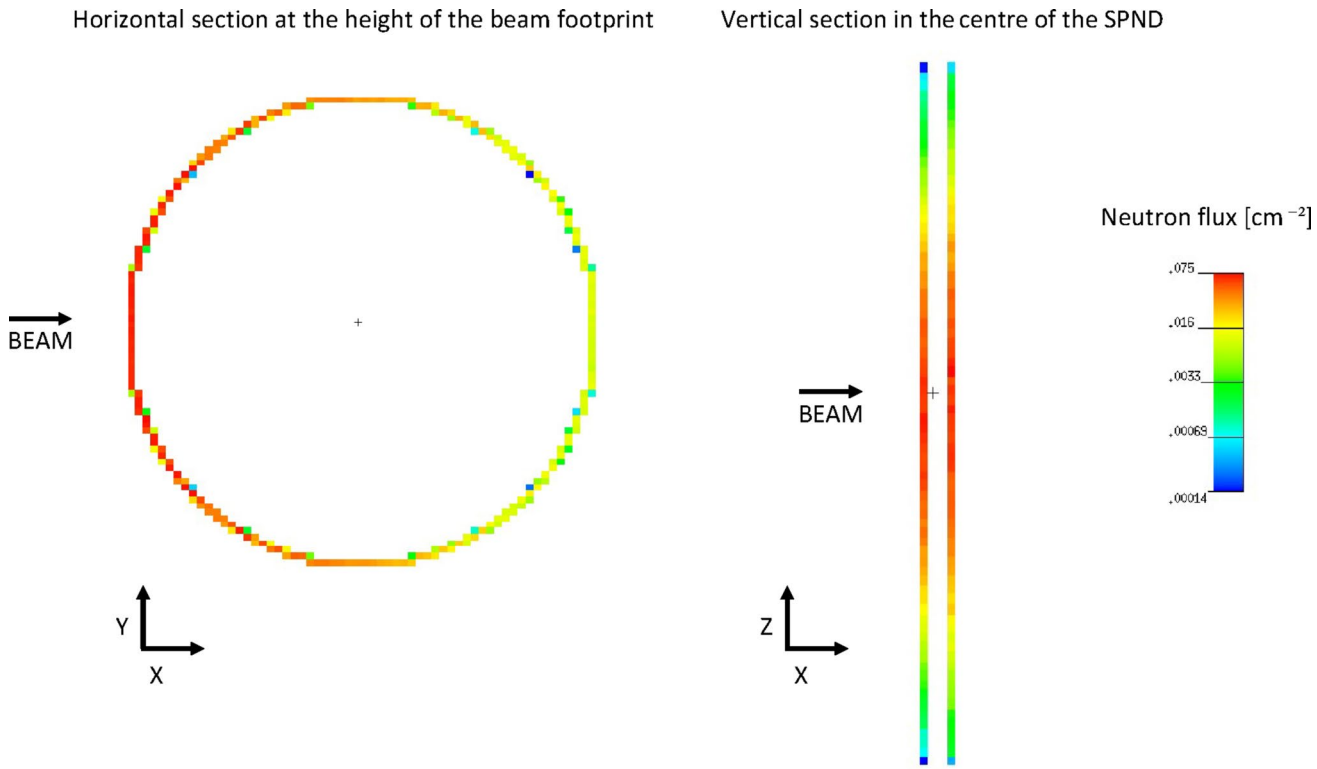

Fig. 8 Neutron source distribution along the height of the SPND and horizontally at the middle of the beam footprint in rig 45 [cm^{-2}]

and photons within the SPND has been obtained using the MCNP WSSA and RSSA cards [29, 30]. Figure 8 illustrates the neutron distribution for the SPND located in rig 45. From this distribution, it can be observed that the neutron field is heterogeneous, influenced by the height of the SPND and the beam footprint size of IFMIF-DONES. Therefore, the calculations have been redone using source data directly from the complete simulation, rather than relying on spectra as an isotropic source. The direction of the neutron distribution in rig 11 is equivalent.

Improvement of the SPND Methodology Used for IFMIF-DONES

To improve the calculation method and to explore a more realistic scenario, the problem is approached differently. Instead of relying on the neutron and gamma spectra at the SPND surface, calculations are now performed directly with the IFMIF-DONES source, which implies the simulation of the deuterons source [6]. With this methodology, the contribution of prompt signals, (γ, e^-) and (n, γ, e^-), is presented jointly.

Using this method, the results for the same cases as before are presented in Table 3. A comparison of the data shows that the values are now smaller than those previously calculated, although they remain in the same order of magnitude. This reduction is due to the more realistic scenario considered, where reactions are less frequent, resulting in a lower current. This is because previously the source was considered isotropic with the particles directed towards the emitter, and now the direction of the particles follows the original trajectory. Nevertheless, the order of magnitude is still sufficient for measurement with an ammeter.

Table 3 Estimated electrical current for the cr and Rh SPNDs in positions rig 45 and 11 with a new methodology. Data are presented in total and by component. The numbers between parentheses indicate the uncertainty

Estimated current [nA]				
Emitter material	Cr		Rh	
Rig	11	45	11	45
(n, β^-)	0.0600(2)	5.800(9)	2.17(1)	20.68(4)
(n, γ, e^-) & (γ, e^-)	4(2)	172(10)	5(2)	215(10)
Total	4(2)	178(10)	7(2)	235(10)

Current values were also estimated for the other HFTM rigs, with Cr values shown in Fig. 9 and Rh values shown in Fig. 10. The data clearly show that the estimated current values for Rh are consistently higher than those for Cr.

Beam Footprint Variation

To assess whether the SPNDs can detect steady-state beam variations, four beam profiles that differ from the IFMIF-EVEDA one but are within the expected range of variation during normal operation were considered.

Fig. 9 Cr SPND estimated signals in each rig position in nA. The numbers between parentheses indicate the uncertainty

	1	2	3	4	5	6	7	8
4	5(2)	18(4)	107(8)	173(10)	178(10)	139(9)	31(4)	8(2)
3	5(2)	18(3)	75(6)	130(8)	137(9)	105(7)	31(4)	9(2)
2	4(2)	15(3)	51(5)	86(7)	92(7)	73(6)	25(4)	8(2)
1	4(2)	12(3)	35(4)	58(5)	56(5)	49(5)	20(3)	7(2)

Fig. 10 Rh SPND estimated signals in each rig position in nA. The numbers between parentheses indicate the uncertainty

	1	2	3	4	5	6	7	8
4	11(2)	34(4)	147(8)	222(10)	235(10)	181(9)	48(5)	14(2)
3	11(2)	32(4)	106(7)	173(9)	181(9)	137(8)	47(4)	15(2)
2	9(2)	25(3)	71(6)	117(7)	123(8)	96(7)	38(4)	14(2)
1	7(2)	19(3)	48(5)	78(6)	75(5)	64(5)	29(3)	12(2)

Fig. 11 Rh SPND estimated signals in each rig position in nA using the HEBT NOMINAL beam profile. The numbers between parentheses indicate the uncertainty

	1	2	3	4	5	6	7	8
4	12(2)	36(4)	144(8)	222(10)	235(10)	170(9)	53(5)	16(3)
3	11(2)	34(4)	106(7)	172(9)	180(9)	132(8)	49(5)	17(3)
2	10(2)	26(3)	74(6)	115(7)	124(7)	94(7)	42(4)	15(2)
1	8(2)	20(3)	48(5)	77(6)	74(5)	62(5)	31(4)	11(2)

Fig. 12 Rh SPND estimated signals in each rig position in nA using the OCTUPOLEX beam profile. The numbers between parentheses indicate the uncertainty

	1	2	3	4	5	6	7	8
4	12(2)	35(4)	154(8)	213(10)	222(10)	193(9)	52(5)	15(3)
3	11(2)	33(4)	111(7)	167(9)	173(9)	142(8)	48(5)	16(2)
2	9(2)	26(3)	75(6)	114(7)	119(7)	99(7)	41(4)	14(2)
1	8(2)	19(3)	50(5)	76(6)	72(5)	64(5)	31(4)	12(2)

Fig. 13 Rh SPND estimated signals in each rig position in nA using the Asymmetric#a beam profile. The numbers between parentheses indicate the uncertainty

	1	2	3	4	5	6	7	8
4	10(2)	30(4)	121(7)	197(10)	245(11)	204(10)	61(5)	18(3)
3	10(2)	29(4)	93(6)	154(8)	182(9)	156(8)	58(5)	19(3)
2	9(2)	23(3)	65(5)	105(7)	127(8)	109(7)	47(5)	16(3)
1	7(2)	16(3)	42(4)	69(6)	76(6)	70(5)	35(4)	13(2)

Fig. 14 Rh SPND estimated signals in each rig position in nA using the Asymmetric#b beam profile. The numbers between parentheses indicate the uncertainty

	1	2	3	4	5	6	7	8
4	13(2)	41(4)	173(9)	235(10)	226(10)	141(8)	44(4)	13(2)
3	12(2)	37(4)	126(8)	179(9)	173(9)	116(7)	41(4)	14(2)
2	11(2)	30(4)	83(6)	122(7)	121(7)	84(6)	35(4)	13(2)
1	9(2)	22(3)	56(5)	80(6)	71(5)	56(5)	26(3)	10(2)

Figures 11, 12, 13 and 14 show the estimated SPND signals for the HEBT NOMINAL, OCTUPOLEX, Asymmetric#a and Asymmetric#b beam profiles, respectively. All calculations were performed using an Rh SPND with the standard beam footprint size and a 40 MeV energy beam.

The estimated signals for SPNDs positioned at the lateral ends of the HFTM show minimal variation with the beam profile. To simplify the analysis, the rigs are grouped into two categories: those located at positive y-coordinates (positive group) and those located at negative y-coordinates (negative group). This division is shown in Fig. 15.

Examining the signal values by group, it can be observed that the rigs in the positive group have the highest signal values for the Asymmetric#a beam profile, while the lowest values are seen for the Asymmetric#b beam profile. This trend is expected as the Asymmetric#a profile enhances the positive group located at positive y-coordinates, whereas the Asymmetric#b profile favours the negative y-coordinates. For this reason, rigs in the negative group show higher signal values for the Asymmetric#b beam profile compared to

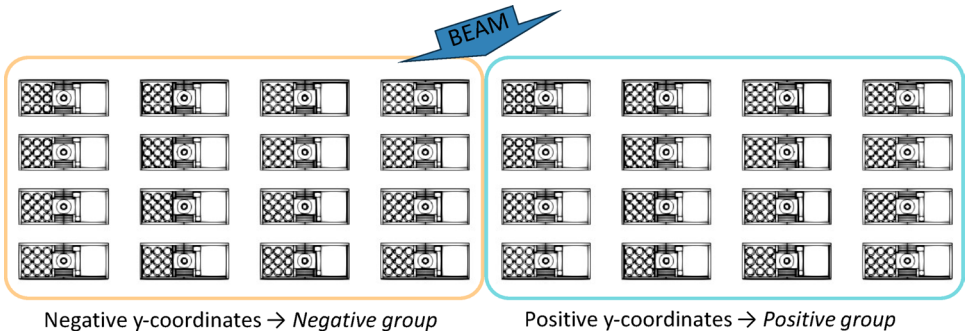

Fig. 15 Division of the HFTM rigs into two groups according to their y-direction coordinate. Rigs located in positive y-coordinates or positive group, and the rigs located in negative y-coordinates or negative group

the Asymmetric#a profile, as the former profile concentrates more power in the negative y-coordinates, corresponding to the rigs in the negative group. Furthermore, for rigs located in the first row of the HFTM, signal variations of up to 30% are estimated, a change that could be detected by the SPND.

However, in the cases of NOMINAL HEBT and OCTUPOLEX beam profiles, there are insufficient differences to identify changes considering the associated uncertainties. It is probably due to the symmetry of these beam profiles and that the SPND cannot identify these types of variations.

Conclusions

This paper outlines the methodology developed to characterise the SPND signals and the validation of the calculation method based on previously published data. Once validated, it is then applied to the irradiation conditions of IFMIF-DONES to estimate the electrical signal that these diagnostics could measure based on its position and emitter material.

For this study, the IFMIF-EVEDA deuteron beam profile was used, assuming a beam footprint of 20×5 cm^2 and a beam energy of 40 MeV. Two methodologies have been carried out, one using the neutron and gamma spectra in the SPND as sources and the other using the deuteron source directly. Consistent but different data have been obtained with both methodologies, as in the first case, the signal is overestimated. In the latter case, beam profiles other than IFMIF-EVEDA have also been used.

The estimated signals are in the nanoampere range and are therefore detectable with standard measurement equipment. In all cases, Rh-based SPNDs consistently produce higher signals than Cr-based ones. Furthermore, the variation of the signal as a function of the position of the SPND suggests that their placement can be optimised for better spatial resolution. When analysing different beam profiles, it is also clear that asymmetries resulting from dynamic beam errors can be detected. These results indicate that SPNDs could be effectively used for online beam monitoring within the HFTM. Nevertheless, additional efforts are needed to improve the predictive capability of this theoretical model by integrating and validating it with experimental measurements.

Acknowledgements This work has been supported by the European Union's FEDER program, SE21 IFMIF-DONES FEDER Junta de Andalucia's program at the Universidad de Granada, by MCIN/AEI/10.13039/501100011033/FEDER, UE (PID2022–137543NB-I00), and has been carried out within the framework of the EUROfusion Consortium, funded by the European Union via the Euratom Research and Training Programme (Grant Agreement No 101052200 — EUROfusion). Views and opinions expressed are however those of the author(s) only and do not necessarily reflect those of the European Union or the European Commission. Neither the European Union nor the European Commission can be held responsible for them. Moreover, this work has been partially supported by the ENEN2plus project (HORIZON-EURATOM-2021-NRT-01-13 101061677) founded by the European Union and by the UGR research project PPJIB2023-092.

Author Contributions I. A and J.A. T wrote the main manuscript text, developed the calculations and prepared figures.M. Anguiano and F. Mota: Funding acquisition, Methodology, Software, Supervision, Validation, Writing –original draft, Writing – review & editing. All authors reviewed the manuscript.

Data Availability No datasets were generated or analysed during the current study.

Declarations

Competing Interests The authors declare no competing interests.

References

1. U. Fischer et al., Neutronic performance issues of the breeding blanket options for the European DEMO fusion power plant. Fusion Eng. Des. **109**(111), 1458–1463 (2016). https://doi.org/10.1016/j.fusengdes.2015.11.051
2. I. Fernández-Berceruelo et al., Alternatives for upgrading the EU DCLL breeding blanket from MMS to SMS. Fusion Eng. Des. **167**, 112–380 (2021). https://doi.org/10.1016/j.fusengdes.2021.112380
3. D. Rapisarda et al., The European dual coolant lithium lead breeding blanket for DEMO: status and perspectives. Nucl. Fusion **61**(11), 115001 (2021). https://doi.org/10.1088/1741-4326/ac26a1
4. J. Knaster et al., The accomplishment of the engineering design activities of IFMIF/EVEDA: the European-Japanese project towards a Li(d,xn) fusion relevant neutron source. Nucl. Fusion (2015). https://doi.org/10.1088/0029-5515/55/8/086003
5. D. Bernardi et al., The IFMIF-DONES project: design status and main achievements within the EUROfusion FP8 work programme. J. Fusion Energy (2022). https://doi.org/10.1007/s10894-022-00337-5
6. Angel, Ibarra et al., 'DONES performance, experimental capabilities and perspectives' Nuclear Fusion, 2025, in press. https://doi.org/10.1088/1741-4326/adcd86
7. Y. Qiu et al., Overview of recent advancements in IFMIF-DONES neutronics activities. Fusion Eng. Des. **201**, 114242 (2024). https://doi.org/10.1016/j.fusengdes.2024.114242
8. Y. Qiu et al., Status of DONES neutronics, source terms analyses and radiation protections. Nucl. Fusion (2025). https://doi.org/10.1088/1741-4326/addeda
9. F. Arbeiter et al., Development and validation status of the IFMIF High Flux Test Module. Fusion Eng. Des. **86**(6–8), 607–610 (2011). https://doi.org/10.1016/j.fusengdes.2011.01.031
10. F. Arbeiter, F. Schwab, 'System Design Description Document (DDD) for the IFMIF-DONES High Flux Test Module (HFTM)', 2020. Accessed: Jul. 12, 2024. https://idm.euro-fusion.org/default.aspx?uid=2N76ET
11. P. Raj, 'Development and Testing of Self–Powered Detectors for Nuclear Measurements in Fusion Reactors', K.I.T. Karlsruhe, 2019. Accessed: Oct. 09, 2024. https://publikationen.bibliothek.kit.edu/1000096884
12. U. Wiącek et al., New approach to the conceptual design of STUMM: A module dedicated to the monitoring of neutron and gamma radiation fields generated in IFMIF-DONES. Fusion Eng. Des. **172**, 112–866 (2021). https://doi.org/10.1016/j.fusengdes.2021.112866
13. S. Becerril-Jarque et al., A real-sized start-up monitoring module prototype for comprehensive test and irradiation campaigns of miniaturized neutron detectors according to the IFMIF-DONES baseline. Nuclear Mater. Energy. **40**, 101–712 (2024). https://doi.org/10.1016/j.nme.2024.101712
14. U. Wiącek et al., STUMM – monitoring module for DONES neutron source – technical challenges. Fusion Eng. Des. **216**, 115–125 (2025). https://doi.org/10.1016/j.fusengdes.2025.115125
15. NIST National Institute of Standards and Technology, 'Atomic Weights and Isotopic Compositions'. Accessed: Feb. 20, 2025. https://physics.nist.gov/cgi-bin/Compositions/stand_alone.pl
16. B.G. Park, D.K. Cho, M.S. Kim, G.D. Kang, *Contribution of External Gamma Rays To SPND at HANARO', in Transactions of the Korean* (Nuclear Society Spring Meeting, Jeju, Korea, May 2014)
17. I. Álvarez et al., Comparative analysis of neutronic features for various specimen payload configurations within the IFMIF-DONES HFTM. Fusion Eng. Des. **210**, 114–729 (2025). https://doi.org/10.1016/j.fusengdes.2024.114729
18. I. Álvarez et al., Assessment of the possibility of irradiating tungsten and Cu-alloys in IFMIF-DONES using a realistic specimens configuration. Nucl. Fusion **65**(2), 026-058 (2025). https://doi.org/10.1088/1741-4326/ada6da
19. L. Vermeeren, 'Neutron and gamma sensitivities of self-powered detectors: Monte Carlo modelling', in 2015 4th International Conference on Advancements in Nuclear Instrumentation Measurement Methods and their Applications (ANIMMA), IEEE, 2015, 1–5. https://doi.org/10.1109/ANIMMA.2015.7465531
20. O. Nomen et al., Preliminary design of the HEBT of IFMIF DONES. Fusion Eng. Des. **153**, 111515 (2020). https://doi.org/10.1016/j.fusengdes.2020.111515
21. J. Molla, O. Nomen, D. Sanchez, C. Oliver, 'Technical Note ENS-6.6.1.0-T14-07 Engineering design of the HEBT magnets 2NT9F2', 2020, Accessed: Mar. 06, 2025. https://idm.euro-fusion.org/default.aspx?uid=2NT9F2
22. Y. Qiu et al., Potential use of IFMIF-DONES target back-plate for material specimens. J. Nucl. Eng. **3**(4), 385–397 (2022). https://doi.org/10.3390/jne3040025
23. Y. Qiu, F. Arbeiter, U. Fischer, F. Schwab, IFMIF-DONES HFTM neutronics modeling and nuclear response analyses. Nucl. Mater. Energy **15**, 185–189 (2018). https://doi.org/10.1016/j.nme.2018.04.009
24. L. Vermeeren, W. Leysen, L. Pichon, V. Salou, G. Helleux, Thermocoax rhodium SPND sensitivity dispersion and validation of the sensitivity calculation model. EPJ Web Conf. **225**, 04015 (2020). https://doi.org/10.1051/epjconf/202022504015
25. H. Lee, S. Choi, K.-H. Cha, K. Lee, D. Lee, New calculational model for self-powered neutron detector based on Monte Carlo simulation. J. Nucl. Sci. Technol. **52**(5), 660–669 (2015). https://doi.org/10.1080/00223131.2014.975766
26. H.D. Warren, Calculational model for self-powered neutron detector. Nucl. Sci. Eng. **48**(3), 331–342 (1972). https://doi.org/10.13182/NSE72-A22491
27. M. Giot et al., Nuclear instrumentation and measurement: a review based on the ANIMMA conferences. EPJ Nuclear Sciences & Technologies **3**, 33 (2017). https://doi.org/10.1051/epjn/2017023
28. L. Barbot, J.-F. Villard, S. Fourrez, L. Pichon, H. Makil, The self-powered detector simulation "MATiSSe" toolbox applied to SPNDs for severe accident monitoring in PWRs. EPJ Web Conf. **170**, 08001 (2018). https://doi.org/10.1051/epjconf/201817008001
29. C.J. Werner et al., MCNP version 6.2 release notes. United States. (2018). https://doi.org/10.2172/1419730
30. J.A. Kulesza et al., 'Title: MCNP® Code Version 6.3.0 Theory & User Manual&#8217
31. 'FENDL-3, 1d: fusion evaluated nuclear data library Ver.3.1d', Accessed: Oct. 09, 2024. https://www-nds.iaea.org/fendl/
32. L. Vermeeren, R. Van Nieuwenhove, Theoretical study of radiation induced electromotive force effects on mineral insulated cables. Rev. Sci. Instrum. **74**(11), 4667–4674 (2003). https://doi.org/10.1063/1.1622976
33. N.P. Goldstein, A monte-Carlo calculation of the neutron sensitivity of self-powered detectors. IEEE Trans. Nucl. Sci. **20**(1), 549–556 (1973). https://doi.org/10.1109/TNS.1973.4326961